

Ternary alkali-metal copper chalcogenides $ACuX$ ($A = \text{Na, K}$ and $X = \text{S, Se, Te}$): Promising candidates for harvesting solar energy

Gurudayal Behera¹, Surabhi Suresh Nair¹, Nirpendra Singh², K.R. Balasubramaniam^{1,*}, and Aftab Alam^{1,†}

¹Department of Energy Science and Engineering, IIT Bombay, Powai, Mumbai 400076, India

²Department of Physics, Khalifa University of Science and Technology, Abu Dhabi 127788, United Arab Emirates

³Department of Physics, Indian Institute of Technology, Bombay, Powai, Mumbai 400076, India

(Received 30 November 2023; revised 22 July 2024; accepted 25 July 2024; published 14 August 2024)

We report a comprehensive first-principles study of the relative stability of the various possible crystal structures, and the electronic and optical properties of ternary alkali-metal copper chalcogenides $ACuX$ ($A = \text{Na/K}$ and $X = \text{S/Se/Te}$) compounds through density functional theory (DFT) calculations. The energetics and phonon spectra of greater than 700 structures were compared, and eight possible stabilized structures of six $ACuX$ compounds were identified using the fixed composition evolutionary search method. Our electronic band structure simulation confirms that all the ternary $ACuX$ compounds are direct-band-gap semiconductors, with the band gap lying between 0.83 to 2.88 eV. These compounds exhibit directly allowed electronic transitions from the valence band to the conduction band, which leads to a significant strength of optical transition probability. This yields a sharp rise in the optical absorption spectra (ranging between 10^4 to 10^5 cm^{-1}) near the energy gap. The estimated spectroscopic limited maximum efficiency (SLME) is about 18% for an 8- μm -thick NaCuTe film. For other $ACuX$ compounds, the SLME ranges between 10% to 13%. In addition, we also explored the feasibility of these ternary $ACuX$ compounds for photocatalytic water-splitting applications and found that they can be promising candidates as photocathodes for hydrogen evolution reactions.

DOI: 10.1103/PhysRevApplied.22.024042

I. INTRODUCTION

In recent years, multinary chalcogenide semiconductors have witnessed extensive applications in the development of thin-film solar photovoltaic (PV) devices. For example, $\text{CuIn}_{1-x}\text{Ga}_x(\text{S, Se})_2$ (CIGS), $\text{Cu}_2\text{ZnSnS}_4$, CdTe, SnS, Sb_2S_3 , etc., have shown immense promise in thin-film solar cells [1–4]. Among them, CdTe and CIGS are most prevalent due to their direct band gaps and high light-absorption capabilities, enabling them to achieve notable solar-cell efficiencies [5–8]. It is however also known that CdTe and CIGS come with certain drawbacks [9–11]. They contain toxic elements, namely Cd and Te, as well as elements that are relatively scarce in the Earth's crust, such as Te, In, and Ga, which is a major concern that could limit market feasibility for sustainable, cost-effective, and large-scale manufacturing. Thus, identifying efficient light-absorber materials in thin-film-based PV devices with band gaps in the visible range is a crucial challenge. Apart from this, there are a few other major issues in existing solar absorbers employed in PV devices,

which are, e.g., organic moieties that cause degradation over short carrier lifetimes (i.e., organic and inorganic halide perovskites [8,12–14]), and the presence of defect states causing a high recombination rate [15,16]. As such, finding alternative materials is the urgent need of the hour. The material should acquire some prerequisite criteria, such as low cost (abundant), high carrier lifetime, high absorption, and defect tolerance.

Recently, alkali-metal ternary telluride $ACuTe$ ($A = \text{Na, K}$) has been proposed to be an efficient light absorber for thin-film solar cells, satisfying most of the above criteria [17]. They are reported to be direct band-gap semiconductors having band-gap values of 1.43 and 1.63 eV for NaCuTe and KCuTe, respectively. The high-absorption coefficient (approximately 10^4 cm^{-1}) in the visible range and a reasonably high carrier lifetime due to low deep-level defects suggest their potentiality as efficient solar absorbers. Additionally, the high abundance of constituent element, i.e., Te is also an added advantage for $ACuTe$ compounds. This has motivated us to further investigate the feasibility of other chalcogenides (S and Se)-based ternary compounds as solar absorbers.

The ternary alkali-metal copper chalcogenides $ACuX$ ($A = \text{Na, K}$ and $X = \text{S, Se, Te}$) have been experimentally

*Contact author: bala.ramanathan@iitb.ac.in

†Contact author: aftab@iitb.ac.in

synthesized by Savelberg and Schfer in 1978 [18,19]. They found that KCuS crystallizes in orthorhombic structure (space group $Pna2_1$), while KCuSe/Te has a hexagonal structure with space group $P6_3/mmc$. Similarly, NaCuSe/Te is reported to crystallize in tetragonal structures with space group $P4/nmm$. Since then, no further experimental as well as theoretical studies have been reported on this class of compounds. Recently, Vaitheeswaran *et al.* [20] studied the structural, electronic, and optical properties of ternary KCuSe and KCuTe using *ab-initio* calculations. They reported these compounds to be semiconductors with suitable band gaps that could be promising as solar absorbers in PV, photodetectors, and other optoelectronic device applications. On a similar line, Boualleg *et al.* [21] reported the phase transition and thermal properties of KCuSe and KCuTe. They reported these two compounds to stabilize in orthorhombic and tetragonal phases, respectively in contrast to the experimental hexagonal structure. The dynamical stability study also confirmed the existence of other possible crystal structures for KCuSe and KCuTe compounds. For other ternary chalcogenides i.e., NaCuSe, NaCuTe, and KCuS, no further studies (both experiment and theory) are reported reassessing their crystal structures. NaCuS is never reported earlier and hence its crystal structure is not known. The conflict between experimental and theoretically predicted crystal structures and the prediction of the most stable structural phases needs to be addressed. In addition, a thorough study to investigate the potential of all these ternary compounds for various solar-harnessing applications can be extremely useful.

In this work, we aim to present a detailed insight into the structural stability, electronic, and optical properties of ternary $ACuX$ compounds assessing their potential as efficient light absorbers using first-principles density functional theory (DFT) calculations. In particular, we utilized a fixed composition evolutionary search algorithm to accurately predict the correct crystal structure of all these six compounds. The method generates greater than 700 structures (depending on the system) and scrutinizes the most stable out of them based on certain factors. This has been a powerful method to predict ground-state structures for a given system. Interestingly, though the crystal structure of a few systems matches with those predicted experimentally, there are other systems where the most stable structure is few meV lower in energy as compared to the experimental ones. Lattice dynamics calculations are also performed in parallel to evaluate the dynamically stable structures for each compound. We further simulated the electronic and optical properties of all six $ACuX$ ($A = \text{Na}/\text{K}$, $X = \text{S}/\text{Se}/\text{Te}$) compounds in their most stable phases. All six $ACuX$ compounds are found to be direct-band-gap semiconductors with band gap values ranging between 0.83 to 2.88 eV. These band-gaps are simulated using the most accurate hybrid

exchange-correlation functional. The optical simulation confirms the anisotropic nature of the absorption spectra having different in-plane and out-of-plane values, with absorption coefficient approximately 10^4 cm^{-1} in the visible range. The theoretically predicted spectroscopic limited maximum efficiency (SLME) is found to lie in the range 10% to 18% for a thickness of 8 to 10 μm under 1-sun illumination AM1.5G. Further, we evaluated the potential of all stable $ACuX$ compounds as photocathodes for water-splitting applications based on their band-edge positions with respect to water redox potential.

II. COMPUTATIONAL DETAILS

The fixed composition evolutionary search algorithm is utilized for predicting the crystal structure, as employed in the USPEX package [22–24]. Initially, 20 structures are generated randomly [23], while the subsequent generations are produced due to variation operators, including heredity (50%), random symmetric structure generation (30%), and soft mutation (20%). The percentage of variation operators is taken after rigorous testing with different variation operators and a review of the existing literature, which produces results that agree with experimental structures [25]. Subsequently, a comprehensive exploration is carried out by generating more than 700 crystal structures depending on the six compounds. Our enthalpy calculations are based on the total ground-state energy without considering the effect of pressure and temperature to identify optimal structures from each generation within the selection criterion. The procedure for local optimization is executed in a five-step process utilizing the generalized gradient approximation (GGA) [26] within the Perdew-Burke-Ernzerhof functional (PBE) [27], implemented in the Vienna *ab initio* simulation package (VASP) [28–30]. The van der Waals interactions are incorporated in all the calculations using the DFT-D3 method of Grimme [31]. For a more accurate calculation of the electronic structure (band gap), the screened hybrid HSE06 functional [32,33] was employed. The kinetic energy cutoff for the plane-wave basis set was set to 520 eV. The Brillouin zone (BZ) integration was performed using a Γ -centered scheme with $12 \times 12 \times 6 k$ meshes for ionic relaxations and $16 \times 16 \times 8$ for self-consistent-field (SCF) calculations for the compounds, which stabilized in hexagonal and tetragonal phases. Similarly, for compounds stabilized in orthorhombic structure, we have used $6 \times 12 \times 12$ and $8 \times 16 \times 16 k$ meshes for ionic relaxations and SCF calculations, respectively. The density of states (DOS) was calculated using the tetrahedron method with Blöch corrections [34]. Electronic band structure within the HSE06 functional was simulated using $8 \times 8 \times 4$ ($4 \times 8 \times 8$) k meshes for hexagonal (orthorhombic) phases, respectively. All the atoms in the unit cell are fully relaxed using the

conjugate gradient method until the force (energy) converges below 0.001 eV/Å (10^{-7} eV). The phonon spectra are calculated using the supercell approach as implemented in the phonopy package [35,36]. The effect of spin-orbit coupling (SOC) was included for all the compounds. Formation energy (ΔE_F) of $ACuX$ (A ; Na/K and X ; S/Se/Te) was calculated using the following expression:

$$\Delta E_F = \frac{E_{\text{Tot}} - [nE_A - lE_{\text{Cu}} - mE_X]}{N}, \quad (1)$$

where “ E_{tot} ” is the total energy of the target compound, “ n ”, “ l ,” and “ m ” are the numbers of Na/K, Cu, and S/Se/Te atoms present in the compound, while N is the total number of atoms present in the cell. E_A , E_{Cu} , and E_X are the total energies per atom of the constituent elements in their respective bulk equilibrium structures.

To simulate the optical properties, the frequency-dependent dielectric constants were calculated within the independent particle approximation (IPA) [37–40], as implemented in VASP. To measure the theoretical maximum possible efficiency, we have used an improved version of the Shockley-Queisser (SQ) efficiency limit known as SLME proposed by Yu *et al.* [41,42] using SL3ME code [43]. More details about the theoretical formulation of optical calculations and SLME can be found in Sec. I within the Supplemental Material [44].

III. RESULTS AND DISCUSSION

A. Energetics and dynamical stability of $ACuX$

Out of all the structures (more than 700 structures) generated by the USPEX package [22–24], we selected nine structures with the lowest formation energies for each ternary $ACuX$ (A = Na, K and X = S, Se, and Te) compounds. The space groups (SG) of these nine structures are $Pnma$, $Pna2_1$, $P6_3/mmc$, $P4/nmm$, $Cmcm$, $P2_1/m$, $F\bar{4}3m$, $P6_3mc$, and $C2/c$, respectively. The prototype crystal structures of such space groups are shown in Fig. S1 within the Supplemental Material [44] and their optimized lattice parameters and corresponding formation energies obtained from DFT calculations for all the six different $ACuX$ compounds are listed in Table S1 to S6 within the Supplemental Material [44]. Table I displays the space group and formation energies (ΔE_F) of the experimentally reported crystal structures and the energetically most stable simulated crystal structures and their energy difference (Δ). $NaCuS$ is one of the compounds that has never been studied before and has been found to stabilize in the space group $Pna2_1$. To further assess its chemical stability, we have calculated its convex hull energy with respect to the other possible secondary phases available in the material project database [45] and open quantum materials database (OQMD) [46]. The majority of these secondary phases reported in these databases are simulated using the PBE exchange-correlation (XC) functional,

TABLE I. Formation energies (ΔE_F) of experimentally reported and theoretically simulated lowest energy structures for six $ACuX$ compounds. “*” indicates the experimentally reported space groups. Δ is the energy difference between the ΔE_F of experimental and theoretical structures.

Compounds	Space Group	ΔE_F (meV/atom)	Δ (meV/atom)
NaCuS	$Pna2_1$	-708	Not synthesized
NaCuSe	$P4/nmm*$ [18]	-617	20
	$P6_3/mmc$	-637	
NaCuTe	$P4/nmm*$ [18]	-493	17
	$P6_3/mmc$	-510	
KCuS	$Pna2_1*$ [19]	-768	
KCuSe	$P6_3/mmc*$	-687	12
	$Pnma$ [18]	-695	
KCuTe	$P6_3/mmc*$ [18]	-595	

which is what we have also used to simulate the target $ACuX$ compounds. The very few secondary phases whose energies were reported using a different XC functional were simulated by PBE and used in the construction of a convex hull energy diagram. The diagram is shown in Fig. 1. Clearly, the $NaCuS$ compound lies on the convex hull region i.e., the lowest ΔE_F region, confirming its chemical stability in the $Pna2_1$ space group as compared to the other secondary phases. However, for the remaining secondary phases, ΔE_F lies above 100 meV/atom and more, indicating their chemical instability (or metastable). Hence, it is reasonable to infer that $NaCuS$ crystallizes in the orthorhombic phase with the $Pna2_1$ space group based on energetics and chemical stability analysis.

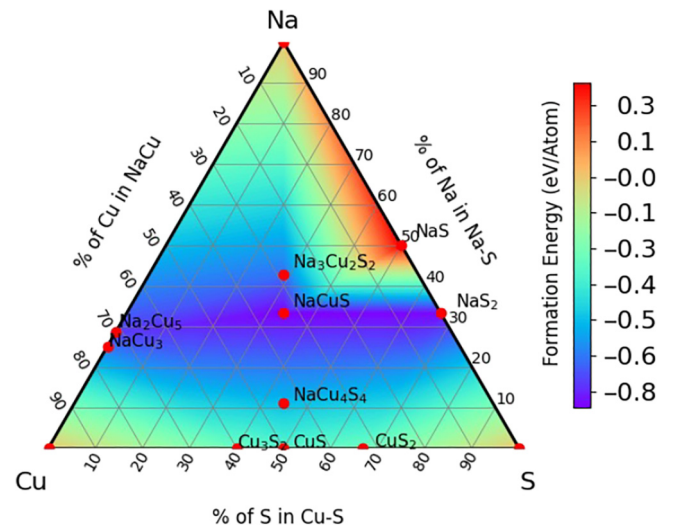


FIG. 1. Convex hull diagram of $NaCuS$ confirming its stability in $Pna2_1$ space group with respect to other secondary phases. Various colors represent the scale of formation energy values, indicated in the adjacent color coding.

Interestingly, for NaCu(Se/Te), energetically they should stabilize in hexagonal structure (SG: $P6_3/mmc$), whose ΔE_F is approximately 17–20 meV/atom lower than those of experimentally reported tetragonal structure (space group $P4/nmm$). KCuS was found to stabilize in the orthorhombic structure having space groups $Pna2_1$, which agrees with the experimental prediction [19]. In contrast, KCuSe is found to stabilize in the orthorhombic crystal structure, which is 12 meV/atom lower in energy than the experimentally reported hexagonal structure [18]. KCuTe stabilizes in the hexagonal structure (SG: $P6_3/mmc$), which matches with the experimental findings [18].

To further assess the phase stability, specially for NaCuSe, NaCuTe, and KCuSe compounds where the experimental structure is higher in energy (by 12 to 20 meV/atom) as compared to the theoretically optimized one, we simulated their phonon dispersion, which will help to evaluate the dynamical stability. The phonon dispersion for all the experimental and theoretically optimized $ACuX$ compounds in different space groups (as shown in Table I) are shown in Fig. S2 within the Supplemental Material [44]. For NaCuS (SG: $Pna2_1$), NaCuSe/Te (SG: $P6_3/mmc$), NaCuSe (SG: $P4/nmm$) and all the KCuX compounds in their respective space groups, the phonon frequencies are found to be nonimaginary, confirming their dynamical stability. A very small imaginary frequency appears at or around the Γ point in the orthorhombic structures of KCuSe (SG: $Pnma$), which may be due to the limited supercell size used in this calculation. Interestingly, the phonon spectrum for the experimentally reported NaCuTe (SG: $P4/nmm$) shows appreciable imaginary frequencies (see Fig. S2(d) within the Supplemental Material [44]), indicating their instability in tetragonal phase. To further check if these negative frequencies are truly real and not arising due to the lack of convergence, we have performed phonon dispersion simulation for NaCuTe using larger supercell size as well as denser k-meshes. We have gone up to a supercell size of $5 \times 5 \times 3$ (unit cell size 450 atoms), yet the imaginary phonon frequencies at both the Γ and A points hardly change. This phonon dispersion with large supercell size is shown in Fig. S3 within the Supplemental Material [44]. To understand the origin of such imaginary frequencies in NaCuTe but not in NaCuSe (both in SG: $P4/nmm$), we have performed a comparative analysis of phonon density of states and the relevant phonon modes in the two cases. Figures S3(b) and S3(f) show the atom projected phonon DOS (PDOS) for NaCuSe and NaCuTe (in $P4/nmm$ space group), respectively. Clearly, NaCuTe shows strong hybridization between Cu and Te in low-frequency range up to 2 THz, while no such hybridization between Cu and Se is observed in the case of NaCuSe. Next, we checked both acoustic and optical phonon modes at Γ point for the two systems. For acoustic phonon modes in NaCuSe and NaCuTe, all atoms (Na, Cu, Se, and Te) exhibit in-phase vibration [see Fig. S3(c) and S3(g) within

the Supplemental Material [44]]. However, a significant difference is observed in the optical phonon modes. In NaCuSe, where there are no imaginary frequencies, all atoms vibrate in phase [see Fig. S3(d) within the Supplemental Material [44]]. In contrast, for NaCuTe, all the atoms (i.e., Cu, Na, and Te) vibrate out of phase, indicating that those imaginary frequencies might be associated with the optical phonon modes [see Fig. S3(h) within the Supplemental Material [44]]. This also hints at the possibility of phase transition, which may stabilize this structure in a nearby minima at elevated temperatures. In addition, it is clear from the phonon dispersion plot of NaCuTe that the optical phonon modes mainly contribute to the imaginary frequencies, while three acoustic modes are nonimaginary. This indicates that it is not an issue with the supercell or k -mesh convergence. As such, we believe that NaCuTe will not stabilize in the tetragonal phase. This brings us to the conclusion that NaCuTe may not crystallize in $P4/nmm$ but in hexagonal crystal structure, i.e., $P6_3/mmc$ space groups, which is favored by both formation energy and phonon dispersion data. We believe the structural characterization of NaCuTe should be revisited. In summary, based on the formation energies and phonon spectra, we have chosen eight of the most stable ternary $ACuX$ compounds, i.e., orthorhombic NaCuS and KCuS (SG: $Pna2_1$), hexagonal NaCuTe and KCuSe/Te (SG: $P6_3/mmc$), tetragonal NaCuSe (SG: $P4/nmm$) and the orthorhombic KCuSe (SG: $Pnma$) to further explore their optoelectronic properties.

B. Electronic structure

All the ternary $ACuX$ compounds were theoretically optimized in their respective stable structures to calculate the electronic properties. The prototype crystal structures are shown in Fig. 2, and the crystallographic parameters, such as lattice constants and bond lengths are tabulated in Table II. The optimized structural details are in fair agreement with the available experimental [18,19] as well as theoretically [17,20,21] reported data. We have also theoretically optimized all the stable $ACuX$ compounds using the PBEsol potential [47], including van der Waals interaction, which is known to predict more accurate structural parameters in comparison with experiment. These results are shown in Table S7 within the Supplemental Material [44]. Clearly, PBEsol+van der Waals lattice parameters compare better with available experimental data. Nonetheless, the electronic structure, including the band topology and band gap does not differ much between PBE and PBEsol-based results [see comparative band structure figures in Fig. S7 within the Supplemental Material [44]]. As such, we believe that the corresponding optoelectronic properties of the studied systems will also not differ much between the two functionals. For $ACuSe/Te$, which stabilizes in the hexagonal structure, Cu and Se/Te ions form

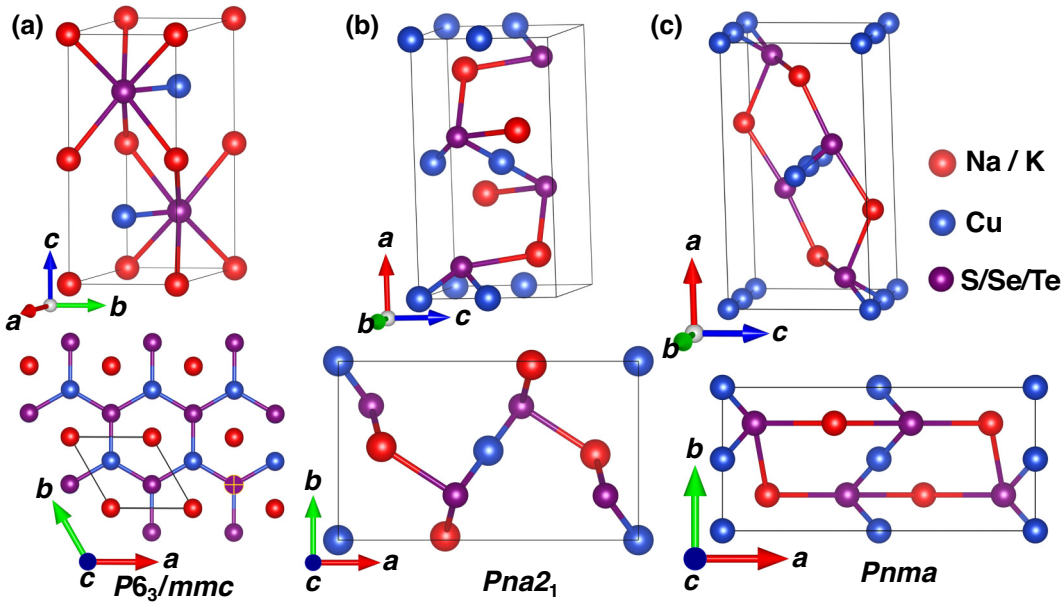


FIG. 2. Prototype crystal structures of $ACuX$ compounds in different space groups, as reported in Table I (a) $ACuX$ ($X = \text{Se}, \text{Te}$) ($P6_3/mmc$), (b) $ACuS$ ($Pna2_1$), (c) $KCuSe$ ($Pnma$), respectively. The set of top and bottom figures indicate the view of the respective structures from (110) and (001) orientations, respectively.

honeycomb (hexagonal) layers along the c direction, and between each hexagonal bilayer, there exists a triangular lattice of Na/K atoms [see Fig. 2(a)]. The Na/K atoms are situated on top of the center of the honeycomb lattice, while Cu/Se/Te atoms are positioned on top of the center of the triangular lattice. In contrast, the lattice arrangement in orthorhombic structures for both the space groups (for $Pna2_1$ and $Pnma$) is slightly different, as shown in Figs. 2(b) and 2(c). In both cases, the $XCuX$ shows a linear chain with an angle of 180° .

The comparative band structure plots with and without spin-orbit coupling (SOC) within the PBE level are shown in Fig. S4 within the Supplemental Material [44]. As evident from Fig. S4 within the Supplemental Material [44], there is no change in band gap as well as band dispersion for S- and Se-based compounds. However, Te, a heavy element, slightly changes the band gap apart from the minor band splitting due to the SOC effect. For instance, E_g for NaCuTe changes from 0.49 eV (w/o SOC) to 0.36 eV (with SOC), and that for KCuTe changes from 0.52 eV (w/o SOC) to 0.41 eV (with SOC) in $P6_3/mmc$ structure. Our PBE-SOC results for KCuSe and KCuTe corroborate well with other theoretical reports [20]. As the SOC effect is not too significant, yet the band gap is conventionally underestimated within the PBE functional, we further performed the electronic structures of all the compounds using HSE06 functional without the SOC effect for more accurate band-gap estimation.

Figure 3 shows the electronic band structures and the optical transition probability of all the $ACuX$ compounds using hybrid (HSE06) functionals. The band structure for

tetragonal NaCuSe is shown in Fig. S8(a) within the Supplemental Material [44]. All the compounds are direct band-gap semiconductors in which the valence-band maximum (VBM) and conduction-band minimum (CBM) are located at Γ point. Table II displays the band-gap (E_g) values simulated using both PBE and HSE06 functionals. We found that the E_g lies in the range 0.83 to 2.88 eV for different compounds. Clearly, E_g for NaCuSe (1.21 eV), KCuSe (1.28 eV), and KCuTe (1.62 eV) are most suitable for photovoltaic applications. It is also observed that the VBM at the Γ point is doubly degenerate for crystal structures belonging to hexagonal symmetry, i.e., $P6_3/mmc$ of $ACu(\text{Se}/\text{Te})$ [Figs. 3(b), 3(c), 3(e), and 3(g)].

Figure 4 shows the orbital projected PDOS for all the $ACuX$ compounds in the respective structures shown in Fig. 2. The PDOS reveals that the VBM mainly consists of the p and d orbitals of Cu and the p orbital of S/Se/Te atoms at or near E_F for all the cases. The CBM is mainly contributed by the s orbital of Na/K, p and d orbitals of Cu, and the s and p orbitals of S/Se/Te, respectively. It is also observed that the electronic states near E_F for alkali metals (Na or K) show a minimal contribution at VBM. The contributions of s orbitals of alkali metals decrease near E_F as we move from $ACuS$ to $ACuSe$ and $ACuTe$. Unlike several other chalcogenide-based compounds, the E_g value in the present case first decreases as we go from Na/KCuS to Na/KCuSe , and then increases for Na/KCuTe . For example, E_g for NaCuS , NaCuSe and NaCuTe are 2.42, 0.83, and 1.21 eV, respectively and a similar trend is obtained for KCuX systems as well. This is mainly attributed to the nature of hybridization

TABLE II. Theoretically optimized lattice parameters, bond lengths, and band gaps of the energetically most stable $ACuX$ ($A = \text{Na, K}; X = \text{S, Se, Te}$) compounds. Experimental results [18,19] are given wherever available.

Compounds	Space group	Lattice constants (\AA)	Bond length (\AA)	Band gap (eV) PBE/HSE06
NaCuS	$Pna2_1$	$a = 9.48, b = 5.65$ $c = 5.13$	Cu—S = 2.17, Na—S = 2.89, 2.79	1.55/2.42
NaCuSe	$P6_3/mmc$	$a = 4.14, c = 8.34$	Cu—Se = 2.39, Na—Se = 3.17	0.02/0.83
	$P4/nmm$	$a = 4.09, c = 6.87$ $a = 4.10, c = 6.82$ (exp. [18])	Cu—Se = 2.56 Na—Se = 2.99	0.04/1.18
NaCuTe	$P6_3/mmc$	$a = 4.42, c = 8.69$	Cu—Te = 2.55, Na—Te = 3.35	0.49/1.21
KCuS	$Pna2_1$	$a = 10.88, b = 6.34,$ $c = 5.34$ $a = 10.66, b = 6.20,$ $c = 5.32$ (exp. [19])	Cu—S = 2.16, K—S = 3.21, 3.19	1.88/2.88
	$Pnma$	$a = 11.84, b = 5.43,$ $c = 6.36$	Cu—Se = 2.28, K—Se = 3.31, 3.39	1.72/2.67
KCuSe	$P6_3/mmc$	$a = 4.20, c = 9.92$ $a = 4.18, c = 9.54$ (exp. [18])	Cu—Se = 2.43, K—Se = 3.47	0.11/1.28
KCuTe	$P6_3/mmc$	$a = 4.48, c = 10.31$ $a = 4.46, c = 9.95$ (exp. [17,18])	Cu—Te = 2.59, K—Te = 3.65	0.52/1.62

between Cu and chalcogen atoms. The electronegativity values for different atoms are $\chi_{\text{Na}} = 0.93$, $\chi_{\text{K}} = 0.82$, $\chi_{\text{Cu}} = 1.9$, and $\chi_{\text{S/Se/Te}} = 2.58/2.55/2.1$, respectively. As chalcogen atoms are more electronegative than alkali

metals, there is always an electronic charge transfer from the Na/K atom to S/Se/Te atoms. Similarly, the charge is also transformed from Cu atoms to S/Se atoms. However, a negligibly small charge transfer between Cu and Te

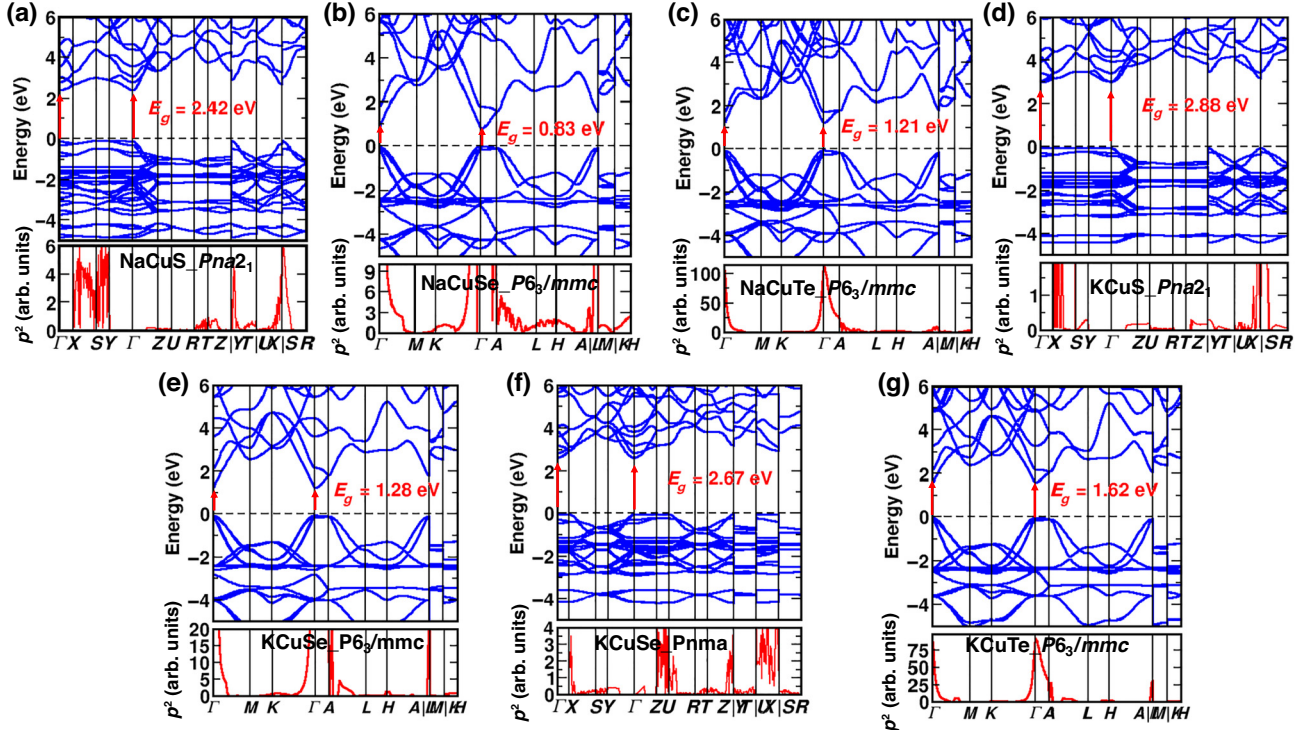


FIG. 3. Electronic band structures (above panels) and optical transition probabilities (square of dipole transition matrix elements) (below panels) of $ACuX$ compounds in their respective lowest energy structure using the HSE06 functional. For KCuSe, results for both $P6_3/mmc$ and $Pnma$ are shown due to a relatively small energy difference between the two. Fermi level (E_F) is set at 0 eV.

atoms can be expected because their electronegativity is almost similar (the difference is 0.2). This is also reflected in their orbital PDOS plots. In order to better understand the role of hybridization in dictating the E_g trend, we show an enlarged view of the orbital projected PDOS above CBM for NaCuS, NaCuSe, and NaCuTe, respectively, in Fig. S5(a)–(c) within the Supplemental Material [44]. A careful inspection of these plots clearly differentiates the orbital hybridization between Cu and S/S/Te atoms at the CBM side. The electronic states of the p and d orbitals of Cu and the p orbitals of S atoms mainly contribute to the CBM side of NaCuS. Similarly, the CBM of NaCuSe consists of the s and d orbitals of Cu and the s orbital of Se. This is mainly attributed to the difference in crystal structures of NaCuS (orthorhombic) and NaCuSe (hexagonal). This leads to an adequate amount of change in bond length between Cu–S(Se) and Na–S(Se) indicating a weak orbital hybridization between them. However, NaCuTe has the same crystal structure as NaCuSe and the nature of orbital hybridization in NaCuTe is quite similar to NaCuSe but different as compared to NaCuS. Also, there is hardly any change in bond length between Cu–Se(Te) and Na–Se(Te). Due to minimal charge transfer between Cu and Te, the orbital contributions from Cu- p , Cu- d , and Te- s are diminished near E_F and indicate only a strong hybridization between Na- s , Cu- s , and Te- p at the CBM side of NaCuTe, causing an increase in the band gap. A similar band-gap trend and the orbital hybridization are also observed between Cu and Te atoms in KCuX compounds [see Fig.

S5(d)–(f) within the Supplemental Material [44]], which can be explained on a similar ground. An analogous band-gap trend is also observed in other chalcogenide-based compounds, such as CdS, CdSe, and CdTe as well as ZnS, ZnSe, and ZnTe, respectively [48–50].

C. Optical properties

The band structure calculations established that all the $ACuX$ compounds are direct band-gap semiconductors, with the band gap falling in the range 0.83 to 2.88 eV. This motivates us to further study the optical properties of these systems and evaluate their efficacy as a solar absorber. Along with the absorption coefficient, we have calculated another screening parameter i.e., SLME proposed by Yu *et al.* [41]. SLME gives an upper bound on the solar efficiency by incorporating the nature and magnitude of the band gap and absorption coefficient for a particular compound. It is an improvised version of the Shockley-Queisser (SQ) efficiency limit. Simulation of SLME also requires information about the possibility of optical transition from VBM to CBM for all the $ACuX$ compounds. To obtain this, we have calculated the transition probability (p^2) by calculating the square of transition dipole-matrix elements. The transition probability for all the $ACuX$ systems is shown in Fig. 3 and Fig. S8(a) within the Supplemental Material [44] (below each band structure plot). Clearly, the direct optical transition from VBM to CBM is allowed for all the hexagonal structures of

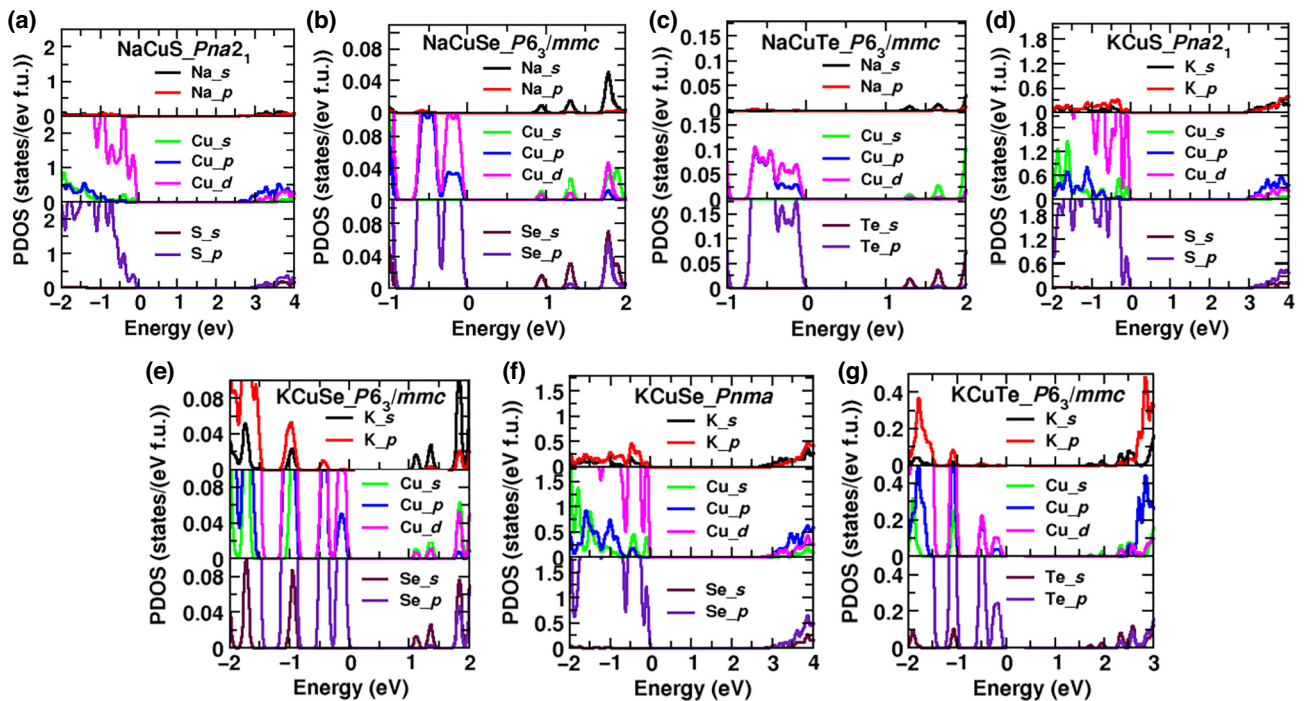


FIG. 4. Orbital projected PDOS for $ACuX$ ($A = \text{Na}, \text{K}$; $X = \text{S}, \text{Se}, \text{Te}$) compounds in the same respective structures as shown in Fig. 3. E_F is set at 0 eV.

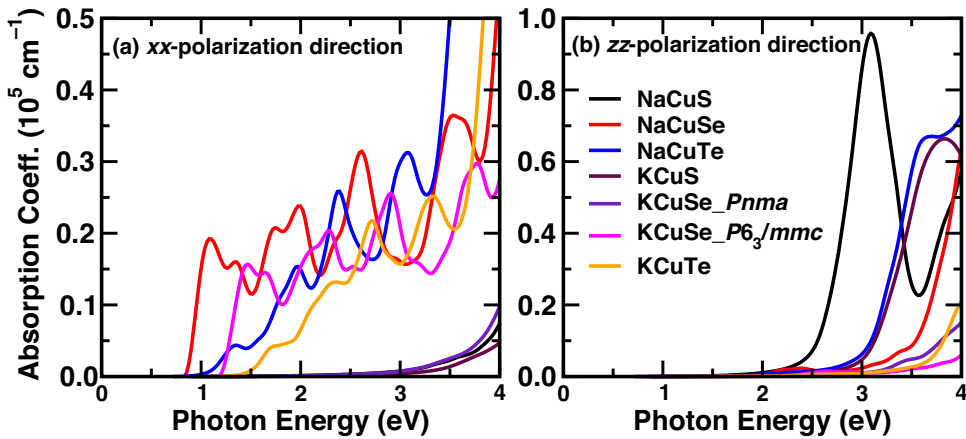


FIG. 5. Absorption coefficient (α) for $ACuX$ ($A = \text{Na}, \text{K}$; $X = \text{S}, \text{Se}, \text{Te}$) along (a) x - and (b) z -polarization directions.

$ACuSe/\text{Te}$ due to the finite p^2 values at the high-symmetry point Γ . The optical transitions are allowed due to the same parity transition of electron states from p states of S/Se/Te atoms at the VBM side to s and p states of Cu at the CBM side and d states of Cu at VBM to s states of S/Se/Te at CBM. In contrast, the p^2 value is found to be zero at Γ point for NaCuS , KCuS , and KCuSe (orthorhombic structures) in Figs. 3(a), 3(d), and 3(f), indicating optically forbidden transition from VBM to CBM.

The absorption coefficient (α) of a given material is a quantifiable descriptor, which dictates the penetration extent of a photon (with a particular wavelength) into the material before it gets absorbed. For a suitable solar absorber, a sharp rise in the absorption coefficient is obtained after the incidence of photon energy closer to its band gap. α is related to the dielectric function and can be calculated using the following expression:

$$\alpha(E) = \frac{\sqrt{2}\omega}{c} \left[\sqrt{\sqrt{\varepsilon_1^2(\omega) + \varepsilon_2^2(\omega)} - \varepsilon_1(\omega)} \right], \quad (2)$$

where E is the incident photon energy, ω is the angular frequency related to photon energy via $E = \hbar\omega$ (\hbar is the reduced Planck constant), and c is the speed of light in vacuum, respectively. ε_1 and ε_2 are the real and imaginary parts of the dielectric function. Figures 5(a) and 5(b) show the absorption spectra plot for all $ACuX$ compounds along the x - (left) and z -polarization (right) directions (arising out of structural anisotropy in hexagonal and orthorhombic structures). For orthorhombic systems (NaCuS , KCuS , KCuSe), the absorption spectra along the y -polarization direction are shown in Fig. S6 within the Supplemental Material [44]. The absorption spectra for tetragonal NaCuSe along xx - and zz -polarization directions are also shown in Fig. S8(b) within the Supplemental Material [44]. The absorption onset for all the compounds are shifted to the band gap obtained

from hybrid calculations. The absorption coefficient of a given material is an essential parameter that determines the extent to which a photon with a particular wavelength can penetrate the material before getting absorbed. In many cases, solar-absorber materials exhibit a sharp rise in the absorption coefficient after the incidence of photon energy closer to its band-gap values. When simulating the absorption coefficient using semilocal functionals, such as LDA or GGA, a pronounced rise in the absorption spectra is observed near the photon energy corresponding to the band-gap values obtained from these potentials. The same calculations, if performed using the hybrid functional, usually yield a similar nature of optical spectra except for the onset of the absorption coefficient, which aligns with the band gap predicted from HSE06 band structure calculations [51–54]. Because the full-fledged optical calculations using the hybrid functional is computationally expensive and we had to perform such calculations for several compounds with different space groups in this work, we used a rigid shift of the absorption spectrum (obtained from our PBE calculation) to match the absorption onset obtained from HSE06 optical calculations. Such a rigid shift does not impact the overall accuracy of the final results. From Figs. 5(a) and 5(b) and Fig. S8(b) within the Supplemental Material [44], it is clear that the absorption coefficients are not same along the three polarization directions because of the associated structural anisotropy. For example, in orthorhombic systems, the absorption coefficient of NaCuS and KCuS is higher (approximately 0.6 to $0.9 \times 10^5 \text{ cm}^{-1}$) along the z -polarization direction than the x and y direction. However, the absorption coefficient of orthorhombic KCuS is high along y -polarization direction with respect to x and z direction (see Fig. S6 within the Supplemental Material [44]). Similarly, for the hexagonal structures, i.e., KCuSe , KCuTe , NaCuSe , and NaCuTe , and tetragonal NaCuSe , the simulated

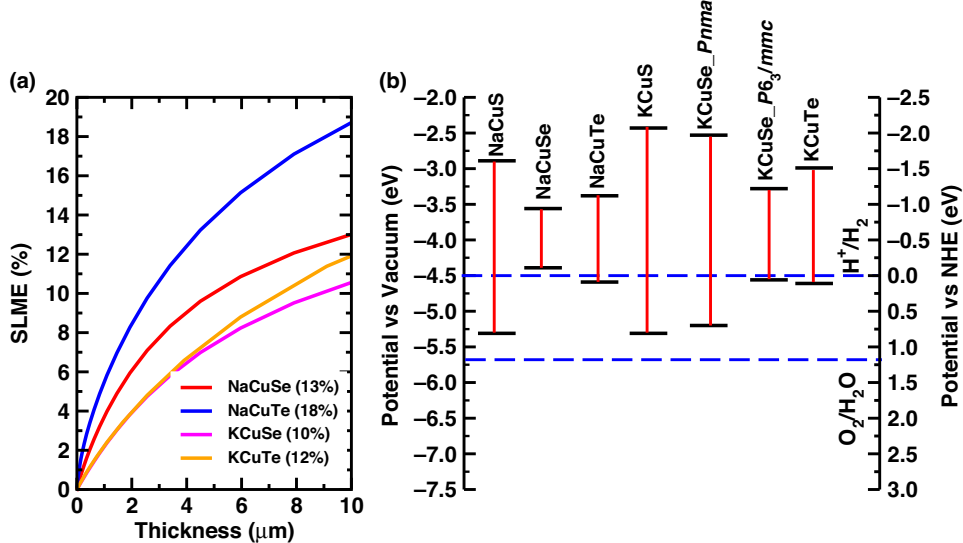


FIG. 6. (a) SLME (at 300 K) vs film thickness for the hexagonal $ACuX$ compounds whose band gaps lie in the visible region. (b) Band edge positions with respect to water redox levels for all stable $ACuX$ compounds.

absorption coefficients fall in the range 0.2×10^5 to $0.6 \times 10^5 \text{ cm}^{-1}$ along x - and y -polarization directions, with a relatively small contribution arising from the z direction as shown in Fig. 5(b).

Next, we have calculated the thickness dependence of SLME of all the $ACuX$ compounds, considering the application for thin-film solar cells. We have chosen four compounds, i.e., hexagonal $ACu(\text{Se}/\text{Te})$ ($A = \text{Na}, \text{K}$) because of their allowed optical transition and high-absorption coefficients in the visible region. The thickness dependence of SLME is shown in Fig. 6(a) and Fig. S8(c) within the Supplemental Material [44]. Clearly, with increasing thickness, the SLME increases and then saturates beyond a certain thickness. The maximum SLME is found to be 18% for a 8 to 10- μm -thick NaCuTe film. Similarly, for the rest of the $ACuX$ systems, the SLME lie between approximately 10 to 13%. Based on the optical and SLME descriptors, it is reasonable to consider that all the selenide- and telluride-based $ACuX$ systems can be potential candidates for light absorbers in solar PV devices.

It is to be noted that all the SLME results shown in this paper are based on the absorption coefficients simulated using the PBE functional with their onset shifted to the HSE06 calculated band-gap value. In general, this SLME value differs only by a few percent as compared with the SLME value simulated using the absorption coefficients obtained from the HSE06 functional. In order to verify the same, we have calculated the SLME using the absorption data from these two sets of calculations for one of our studied compounds, KCuTe . The comparative SLME vs film thickness plot is shown in Fig. S9 with the Supplemental Material [44]. As evident from the figure, there is hardly any change in SLME (nearly 1 to 1.5% change) in very thin

films up to 4 to 5 μm , which is the range usually targeted for thin-film PV devices. However, the difference in SLME increases to 3–4% for higher thicknesses. For example, for films with thickness lying between 8 to 10 μm , the SLME difference between the two methods ranges from 4–5%.

D. Potential application in photoelectrochemical (PEC) water splitting

We further investigate the feasibility of the ternary $ACuX$ compounds for photocatalytic water-splitting applications. In order to obtain the exact band edge positions, one should align the energy levels of both the bulk and surfaces to a common reference point. To achieve this, we adopted an approach utilizing core energy levels and vacuum potential levels as suitable references, enabling the determination of surface band bending with respect to bulk band positions [55–57]. We calculated the electrostatic potential along the (001) plane of the $ACuX$ surface slabs with 20 Å vacuum for the obtained external vacuum level as a reference. Core level calculations with the bulk and surface unit cells were done, selecting the Na-1s and K-1s levels as representative core levels for NaCuX - and KCuX -based compounds to estimate the absolute energy levels. The absolute valence- and conduction-band edge positions (E_{VBM} and E_{CBM}) were then calculated using the expression [58–60]:

$$E_{\text{VBM/CBM}} = \epsilon_{\text{VBM/CBM}}^{\text{KS}} - (E_{\text{core-1s}}^{\text{bulk}} - E_{\text{core-1s}}^{\text{surface}}) - E_{\text{vac}} \quad (3)$$

where $\epsilon_{\text{VBM/CBM}}^{\text{KS}}$ is the Kohn-Sham (KS) eigenvalue in the bulk phase corresponding to the band. $E_{\text{core-1s}}^{\text{bulk}}$ and $E_{\text{core-1s}}^{\text{surface}}$ are the average Na/K 1s core level energies in the

bulk and innermost layer of the surface slab, respectively, and E_{vac} is the vacuum level obtained from the planar average electrostatic potential. Figure 6(b) shows the band edge positions for all the stable $ACuX$ compounds with respect to vacuum as well as normal hydrogen electrode (NHE). For a compound to be promising for PEC water splitting, the CBM must locate more negative than the redox potential of H^+/H_2 (0 V vs NHE), and the VBM must align more positive than the redox potential of O_2/H_2O (1.23 V vs NHE) at ambient conditions [61]. As evident from Fig. 6(b), all ternary copper chalcogenides exhibit well-positioned conduction-band edges suitable for use as photocathodes for the hydrogen evolution reaction (HER) in a PEC cell.

Apart from the promising optoelectronic features, we have also observed flat valence-band edges for all $ACuX$ compounds (see Fig. 3). The presence of flat bands results in high effective mass with a large density of states. Such flat bands are extremely useful to achieve a high Seebeck coefficient and hence, beneficial for thermoelectric applications. Additionally, some of these chalcogenides are found to acquire large band gap (e.g., 2.88 eV for $KCuS$, 2.67 eV for $KCuSe$, 2.42 eV for $NaCuS$), which along with promising optical properties (absorption, carrier mobility, etc.) can be useful for light-emitting diodes and transparent conductor-based applications.

IV. CONCLUSION

In conclusion, we have systematically investigated the chemical and dynamical stability and optoelectronic properties of ternary $ACuX$ ($A = Na, K; X = S, Se, Te$) chalcogenides using first-principles calculations. The structural stability metrics ensure that $NaCuS$, $KCuS$, and $KCuSe$ crystallize in orthorhombic structure while $NaCuSe/Te$ and $KCuTe$ stabilize in the hexagonal phase. Interestingly, the hexagonal structure of $NaCuSe$ is likely to have an energy minima very close to a tetragonal phase, and hence might have strong competition in its formation depending on the synthesis procedure. Interestingly, few of these compounds show intriguing energetics and phonon trends, which suggests they stabilize in the structure(s) other than that predicted experimentally (one report only). This demands a revisit of the crystal structure prediction. All the compounds are direct band-gap semiconductors having band gaps laying between 0.83 to 2.88 eV. The direct optical transitions are forbidden for orthorhombic systems ($NaCuS$, $KCuS$, and $KCuSe$), while it is allowed for the remaining systems (hexagonal phase). The absorption coefficient for the optically allowed $ACuX$ compounds lie in the range approximately $(0.2 \text{ to } 0.6) \times 10^5 \text{ cm}^{-1}$ in the visible region. The highest simulated efficiency for the $NaCuTe$ is determined to be 18% for an 8 μm thick film. In addition, the favorable straddling of valence-band edges with respect to the normal hydrogen electrodes confirms

the suitability of all these compounds as photocathodes for the hydrogen evolution reaction (HER) in the photoelectrochemical (PEC) process. The present study suggests that the ternary alkali-metal-based copper chalcogenides can be suitable candidates as light absorbers in PV cells as well as photocathodes for HER in photocatalytic water-splitting applications, requiring further experimental investigation.

ACKNOWLEDGMENTS

G.B. would like to thank the Council of Scientific and Industrial Research (CSIR), India, for providing senior research fellowship. N.S. acknowledges the financial support from the Khalifa University of Science and Technology under the Emerging Science & Innovation Grant No. ESIG-2023-004 and the contribution of Khalifa University's high-performance computing and research computing facilities to the results of this research.

- [1] Bayram Saparov, Next generation thin-film solar absorbers based on chalcogenides, *Chem. Rev.* **122**, 10575 (2022).
- [2] Soubantika Palchoudhury, Karthik Ramasamy, and Arunava Gupta, Multinary copper-based chalcogenide nanocrystalline systems from the perspective of device applications, *Nanoscale Adv.* **2**, 3069 (2020).
- [3] Donghyeop Shin, Bayrammurad Saparov, and David B. Mitzi, Defect engineering in multinary earth-abundant chalcogenide photovoltaic materials, *Adv. Energy Mater.* **7**, 1602366 (2017).
- [4] Indu Sharma, Pravin S. Pawar, Rahul Kumar Yadav, Raju Nandi, and Jaeyeong Heo, Review on bandgap engineering in metal-chalcogenide absorber layer via grading: A trend in thin-film solar cells, *Sol. Energy* **246**, 152 (2022).
- [5] Albert Polman, Mark Knight, Erik C. Garnett, Bruno Ehrler, and Wim C. Sinke, Photovoltaic materials: Present efficiencies and future challenges, *Science* **352**, aad4424 (2016).
- [6] A. Green Martin, Emery Keith, Hishikawa Yoshihiro, and Warta Wilhelm, Solar cell efficiency tables (version 33), *Prog. Phot.: Res. Appl.* **17**, 85 (2008).
- [7] S. Ouendadji, S. Ghemid, H. Meradji, and F. El Haj Hassan, Theoretical study of structural, electronic, and thermal properties of CdS , $CdSe$ and $CdTe$ compounds, *Comput. Mater. Sci.* **50**, 1460 (2011).
- [8] Sergey Eyderman, Alexei Deinega, and Sajeet John, Near perfect solar absorption in ultra-thin-film GaAs photonic crystals, *J. Mater. Chem. A* **2**, 761 (2014).
- [9] Séan R. Kavanagh, Aron Walsh, and David O. Scanlon, Rapid recombination by cadmium vacancies in $CdTe$, *ACS Energy Lett.* **6**, 1392 (2021).
- [10] Baoying Dou, Stefano Faletta, Jörg Neugebauer, Christoph Freysoldt, Xie Zhang, and Su-Huai Wei, Chemical trend of nonradiative recombination in $Cu(In, Ga)Se_2$ alloys, *Phys. Rev. Appl.* **19**, 054054 (2023).
- [11] Robert B. Wexler, Gopalakrishnan Sai Gautam, and Emily A. Carter, Optimizing kesterite solar cells from Cu_2ZnSnS_4 to $Cu_2CdGe(S, Se)_4$, *J. Mater. Chem. A* **9**, 9882 (2021).

- [12] Samuel D. Stranks, Giles E. Eperon, Giulia Grancini, Christopher Menelaou, Marcelo J. P. Alcocer, Tomas Leijtens, Laura M. Herz, Annamaria Petrozza, and Henry J. Snaith, Electron-hole diffusion lengths exceeding 1 μm in an organometal trihalide perovskite absorber, *Science* **342**, 341 (2013).
- [13] X. J. Liu, K. Matsuda, Y. Moritomo, A. Nakamura, and N. Kojima, Electronic structure of the gold complexes $\text{Cs}_2\text{Au}_2X_6$ ($X = \text{I}, \text{Br}$, and Cl), *Phys. Rev. B* **59**, 7925 (1999).
- [14] Wei E. I. Sha, Xingang Ren, Luzhou Chen, and Wallace C. H. Choy, The efficiency limit of $\text{CH}_3\text{NH}_3\text{PbI}_3$ perovskite solar cells, *Appl. Phys. Lett.* **106**, 221104 (2015).
- [15] Samuel D. Stranks, Victor M. Burlakov, Tomas Leijtens, James M. Ball, Alain Goriely, and Henry J. Snaith, Recombination kinetics in organic-inorganic perovskites: Excitons, free charge, and subgap states, *Phys. Rev. Appl.* **2**, 034007 (2014).
- [16] Wolfgang Tress, Juan Pablo Correa Baena, Michael Saliba, Antonio Abate, and Michael Graetzel, Inverted current–voltage hysteresis in mixed perovskite solar cells: Polarization, energy barriers, and defect recombination, *Adv. Energy Mater.* **6**, 1600396 (2016).
- [17] Diana Dahliah, Guillaume Brunin, Janine George, Viet-Anh Ha, Gian-Marco Rignanese, and Geoffroy Hautier, High-throughput computational search for high carrier lifetime, defect-tolerant solar absorbers, *Energy Environ. Sci.* **14**, 5057 (2021).
- [18] Gerhard Savelsberg, Ternäre Pnictide und Chalkogenide von Alkalimetallen und IB-bzw. IIB-Elementen/On ternary pnictides and chalkogenides of alkaline metals and IB-resp. II B-elements, *Z. Naturforsch. B* **33**, 370 (1978).
- [19] Gerhard Savelsberg and Herbert Schäfer, Darstellung und Kristallstruktur von Na_2AgAs und KCuS /Preparation and crystal structure of Na_2AgAs and KCuS , *Z. Naturforsch. B* **33**, 711 (1978).
- [20] Atahar Parveen and G. Vaitheeswaran, Exploring exemplary optoelectronic and charge transport properties of KCuX ($X = \text{Se}, \text{Te}$), *Sci. Rep.* **8**, 1 (2018).
- [21] M. Boualleg, B. Bennecer, and F. Kalarasse, Ab initio predictions of structures and physical properties of the KCuX ($X = \text{Se}$ and Te) phases under pressure, *Comput. Condens. Matter* **30**, e00616 (2022).
- [22] Artem R. Oganov, Andriy O. Lyakhov, and Mario Valle, How evolutionary crystal structure prediction works- and why, *Acc. Chem. Res.* **44**, 227 (2011).
- [23] Andriy O. Lyakhov, Artem R. Oganov, Harold T. Stokes, and Qiang Zhu, New developments in evolutionary structure prediction algorithm USPEX, *Comput. Phys. Commun.* **184**, 1172 (2013).
- [24] Artem R. Oganov and Colin W. Glass, Crystal structure prediction using ab initio evolutionary techniques: Principles and applications, *J. Chem. Phys.* **124**, 244704 (2006).
- [25] Qiang Zhu, Vinit Sharma, Artem R. Oganov, and Ramamurthy Ramprasad, Predicting polymeric crystal structures by evolutionary algorithms, *J. Chem. Phys.* **141**, 154102 (2014).
- [26] John P. Perdew, Kieron Burke, and Matthias Ernzerhof, Generalized gradient approximation made simple, *Phys. Rev. Lett.* **78**, 1396 (1997).
- [27] John P. Perdew, Kieron Burke, and Matthias Ernzerhof, Generalized gradient approximation made simple, *Phys. Rev. Lett.* **77**, 3865 (1996).
- [28] Georg Kresse and Jürgen Furthmüller, Efficiency of ab initio total energy calculations for metals and semiconductors using a plane-wave basis set, *Comput. Mater. Sci.* **6**, 15 (1996).
- [29] Georg Kresse and Jürgen Hafner, Ab initio molecular dynamics for liquid metals, *Phys. Rev. B* **47**, 558 (1993).
- [30] Georg Kresse and Jürgen Furthmüller, Efficient iterative schemes for ab initio total-energy calculations using a plane-wave basis set, *Phys. Rev. B* **54**, 11169 (1996).
- [31] Stefan Grimme, Semiempirical GGA-type density functional constructed with a long-range dispersion correction, *J. Comput. Chem.* **27**, 1787 (2006).
- [32] Jochen Heyd, Gustavo E. Scuseria, and Matthias Ernzerhof, Hybrid functionals based on a screened coulomb potential, *J. Chem. Phys.* **118**, 8207 (2003).
- [33] Jochen Heyd and Gustavo E. Scuseria, Efficient hybrid density functional calculations in solids: Assessment of the Heyd–Scuseria–Ernzerhof screened coulomb hybrid functional, *J. Chem. Phys.* **121**, 1187 (2004).
- [34] Peter E. Blöchl, Ove Jepsen, and Ole Krogh Andersen, Improved tetrahedron method for Brillouin-zone integrations, *Phys. Rev. B* **49**, 16223 (1994).
- [35] A. Togo and I. Tanaka, First principles phonon calculations in materials science, *Scr. Mater.* **108**, 1 (2015).
- [36] K. Parlinski, Z. Q. Li, and Y. Kawazoe, First-principles determination of the soft mode in cubic ZrO_2 , *Phys. Rev. Lett.* **78**, 4063 (1997).
- [37] M. Gajdoš, K. Hummer, G. Kresse, J. Furthmüller, and F. Bechstedt, Linear optical properties in the projector-augmented wave methodology, *Phys. Rev. B* **73**, 045112 (2006).
- [38] Stephen L. Adler, Quantum theory of the dielectric constant in real solids, *Phys. Rev.* **126**, 413 (1962).
- [39] Nathan Wiser, Dielectric constant with local field effects included, *Phys. Rev.* **129**, 62 (1963).
- [40] M. S. Dresselhaus, *Solid State Physics Part II Optical Properties of Solids*, Vol. 17, Lecture Notes (Massachusetts Institute of Technology, Cambridge, MA, 2001), p. 15.
- [41] Liping Yu and Alex Zunger, Identification of potential photovoltaic absorbers based on first-principles spectroscopic screening of materials, *Phys. Rev. Lett.* **108**, 068701 (2012).
- [42] T. O. M. Tiedje, E. L. I. Yablonovitch, George D. Cody, and Bonnie G. Brooks, Limiting efficiency of silicon solar cells, *IEEE Trans. Electron Devices* **31**, 711 (1984).
- [43] Marnik Bercx, Rolando Saniz, Bart Partoens, and Dirk Lamoen, in *Many-body Approaches at Different Scales: A Tribute to Norman H. March on the Occasion of his 90th Birthday* (Springer, 2018), p. 177.
- [44] See Supplemental Material at <http://link.aps.org/supplemental/10.1103/PhysRevApplied.22.024042>, which includes Refs. [37–42], for further theoretical backgrounds, the formation energies in for different space-group lattices of the ACuX compound and their phonon-dispersion plots for the energetically most stable structures, comparison of the crystal structures PBE vs PBESol+VdW, SOC

- band structures and absorption spectra of orthorhombic structures along yy -polarization direction.
- [45] Anubhav Jain, Shyue Ping Ong, Geoffroy Hautier, Wei Chen, William Davidson Richards, Stephen Dacek, Shreyas Cholia, Dan Gunter, David Skinner, Gerbrand Ceder, *et al.*, Commentary: The Materials Project: A materials genome approach to accelerating materials innovation, *APL Mater.* **1**, 011002 (2013).
- [46] Scott Kirklin, James E. Saal, Bryce Meredig, Alex Thompson, Jeff W. Doak, Muratahan Aykol, Stephan Rühl, and Chris Wolverton, The Open Quantum Materials Database (OQMD): Assessing the accuracy of DFT formation energies, *npj Comput. Mater.* **1**, 1 (2015).
- [47] John P. Perdew, Adrienn Ruzsinszky, Gábor I. Csonka, Oleg A. Vydrov, Gustavo E. Scuseria, Lucian A. Constantin, Xiaolan Zhou, and Kieron Burke, Restoring the density-gradient expansion for exchange in solids and surfaces, *Phys. Rev. Lett.* **100**, 136406 (2008).
- [48] Engin Deligoz, Kemal Colakoglu, and Yasemin Ciftci, Elastic, electronic, and lattice dynamical properties of CdS, CdSe, and CdTe, *Phys. B: Condens. Matter* **373**, 124 (2006).
- [49] Y. Duan and M. Jungen, Electronic structural and magnetic properties of cadmium chalcogenide beryllosilicate sodalites, *Eur. Phys. J. B* **2**, 183 (1998).
- [50] Oleg Zakharov, Angel Rubio, Xavier Blase, Marvin L. Cohen, and Steven G. Louie, Quasiparticle band structures of six II-VI compounds: ZnS, ZnSe, ZnTe, CdS, CdSe, and CdTe, *Phys. Rev. B* **50**, 10780 (1994).
- [51] Deobrat Singh, Sanjeev K. Gupta, Igor Lukačević, Matko Mužević, Yogesh Sonvane, and Rajeev Ahuja, Effect of electric field on optoelectronic properties of indiene monolayer for photoelectric nanodevices, *Sci. Rep.* **9**, 17300 (2019).
- [52] Xuefei Liu, Zhaocai Zhang, Bing Lv, Zhao Ding, and Zijiang Luo, Impact of the vertical strain on the Schottky barrier height for graphene/AlN heterojunction: A study by the first-principles method, *Eur. Phys. J. B* **94**, 1 (2021).
- [53] Mitsutoshi Nishiwaki and Hiroyuki Fujiwara, Highly accurate prediction of material optical properties based on density functional theory, *Comput. Mater. Sci.* **172**, 109315 (2020).
- [54] R. Del Sole and Raffaello Girlanda, Optical properties of semiconductors within the independent-quasiparticle approximation, *Phys. Rev. B* **48**, 11789 (1993).
- [55] Taehun Lee, Yonghyuk Lee, Woosun Jang, and Aloysisus Soon, Understanding the advantage of hexagonal WO_3 as an efficient photoanode for solar water splitting: A first-principles perspective, *J. Mater. Chem. A* **4**, 11498 (2016).
- [56] Andrew J. Logsdail, David O. Scanlon, C. Richard, A. Catlow, and Alexey A. Sokol, Bulk ionization potentials and band alignments from three-dimensional periodic calculations as demonstrated on rocksalt oxides, *Phys. Rev. B* **90**, 155106 (2014).
- [57] Keith T. Butler and John H. Harding, A computational investigation of nickel (silicides) as potential contact layers for silicon photovoltaic cells, *J. Phys. Condens. Matter.* **25**, 395003 (2013).
- [58] Chol-Hyok Ri, Yun-Sim Kim, Un-Gi Jong, Yun-Hyok Kye, Se-Hun Ryang, and Chol-Jun Yu, First-principles study on structural, electronic and optical properties of perovskite solid solutions $\text{KB}_{1-x}\text{Mg}_x\text{I}_3$ ($B = \text{Ge}, \text{Sn}$) toward water splitting photocatalysis, *RSC Adv.* **11**, 26432 (2021).
- [59] Young-Kwang Jung, Ji-Hwan Lee, Aron Walsh, and Aloysisus Soon, Influence of Rb/Cs cation-exchange on inorganic Sn halide perovskites: From chemical structure to physical properties, *Chem. Mater.* **29**, 3181 (2017).
- [60] Un-Gi Jong, Chol-Jun Yu, Yun-Hyok Kye, Yong-Guk Choe, Wei Hao, and Shuzhou Li, First-principles study on structural, electronic, and optical properties of inorganic Ge-based halide perovskites, *Inorg. Chem.* **58**, 4134 (2019).
- [61] Vidhya Chakrapani, John C. Angus, Alfred B. Anderson, Scott D. Wolter, Brian R. Stoner, and Gamini U. Sumanasekera, Charge transfer equilibria between diamond and an aqueous oxygen electrochemical redox couple, *Science* **318**, 1424 (2007).